A sliding mode observer approach to oscillatory fault detection in commercial aircraft

Keijzer, T.; Engelbrecht, J. A.A.; Goupil, P.; Ferrari, R. M.G.

DOI
10.1016/j.conengprac.2023.105719

Publication date
2023

Document Version
Final published version

Published in
Control Engineering Practice

Control Engineering Practice 141 (2023) 105719

Contents lists available at ScienceDirect

Control Engineering Practice

journal homepage: www.elsevier.com/locate/conengprac

A sliding mode observer approach to oscillatory fault detection in commercial aircraft

T. Keijzer [a], J.A.A. Engelbrecht [b], P. Goupil [c], R.M.G. Ferrari [a,*]

[a] Delft Center for Systems and Control, Delft University of Technology, The Netherlands
[b] Department of E&E Engineering, Stellenbosch University, South Africa
[c] Flight Control System, Airbus France, 316 Route de Bayonne, 31060 Toulouse Cedex 09, France

ARTICLE INFO

Keywords:
Oscillatory failure case
Fault detection
Sliding mode observer
Experimental data

ABSTRACT

The Flight Control System (FCS) is one of the most important systems in all modern aircraft. For such systems it is required to have robust Fault Detection Isolation and Reconfiguration (FDIR) functionalities with high detection performance. In this work we specifically consider the Oscillatory Failure Cases (OFC), which, if not mitigated, can cause additional structural loads for which the aircraft is not designed. A Sliding Mode Observer (SMO) based detection method is proposed for fast and consistent detection of these OFC faults. A benchmark of a generic aircraft FCS equipped with OFC simulation capabilities, as well as the presented solution for detection, have previously been presented within a competition at the 2020 IFAC World Congress.

1. Introduction

The design of a commercial aircraft is a complex procedure involving many different requirements, but a common factor throughout it is the aim to minimize weight to obtain better fuel efficiency in operation. In this context, the aircraft is supported by a flexible structure that is designed to withstand a specified load envelope with minimal structural reinforcements. The load envelope specification is normally based on the expected loads on the aircraft resulting from atmospheric effects (such as turbulence) and maneuvers performed by the aircraft itself. However, certain system faults can lead to additional structural loads which must also be considered when performing the aircraft design. These additional loads require extra structural reinforcements which increases the mass and reduces the fuel efficiency. A particular type of system fault that only occurs rarely, but causes significant structural loads is the Oscillatory Failure Case (OFC) (Besch, Giesseler, & Schuller, 1996; Goupil, 2010). An OFC is an unwanted oscillation of a control surface which is caused by the propagation of a spurious oscillatory signal inside the servo control loop of a fly-by-wire flight control system of a commercial aircraft. It is generally due to a fault affecting an electronic component or a mechanical breakage.

If an OFC could be quickly and robustly detected and accommodated, before it causes additional structural loads, the additional structural reinforcements would not be necessary, thus saving mass, increasing fuel efficiency, and easing installation constraints. Such a goal can be attained by employing Fault Detection, Identification and Reconfiguration (FDIR) methodologies. FDIR constitutes a large and active field of research as attested by many surveys that have been published from 1990 (Frank, 1990) up to recent years (Chen, Jiang, Ding, & Huang, 2022; Chi, Dong, Wang, Yu, & Leung, 2022; Hwang, Kim, Kim, & Seah, 2010; Song & He, 2022; Tipaldi & Bruenjes, 2015; Yutian, Changgang, & Junjie, 2010). The first research works on OFC detection were conducted in the 90's (Besch et al., 1996) and describe an oscillatory failure identification system (OFIS) that uses several combinations of linear methods and signal processing techniques where one method corresponds to one fault scenario. Since these first works, the OFC detection problem has gained significant interest and a wide range of approaches have been tested and published. Part of the current industrial state of practice has been published by Airbus in 2010 (Goupil, 2010). Non-linear filtering techniques have been widely used and assessed in the industrial sector (Alcorta-Garcia, Zolghadri, & Goupil, 2011; Lavigne, Zolghadri, Goupil, & Simon, 2011) and they are now fully part of the most recent industrial state of practice (Zolghadri, Henry, Cieslak, Efimov, & Goupil, 2013) with a certified solution embedded and flying on the Airbus A350 long range aircraft.

Pons et al. applied a learning approach based on interval analysis to OFC identification (Pons, Jauberthie, Travé-Massuyès, & Goupil, 2008). Varga and Ossmann (2012) developed a linear parameter-varying (LPV) based identification approach for oscillatory failure cases. Due to the oscillatory nature of the fault to detect, differentiator approaches have been successfully applied and tested on real data (Cieslak, Efimov, Zolghadri, Henry, & Goupil, 2013; Efimov, Cieslak, Zolghadri, & Henry, 2013). Sifi, Lavigne, Cazaurang, and Goupil

* Corresponding author.
E-mail address: r.ferrari@tudelft.nl (R.M.G. Ferrari).

https://doi.org/10.1016/j.conengprac.2023.105719
Received 31 March 2023; Received in revised form 19 August 2023; Accepted 19 September 2023
Available online 10 October 2023

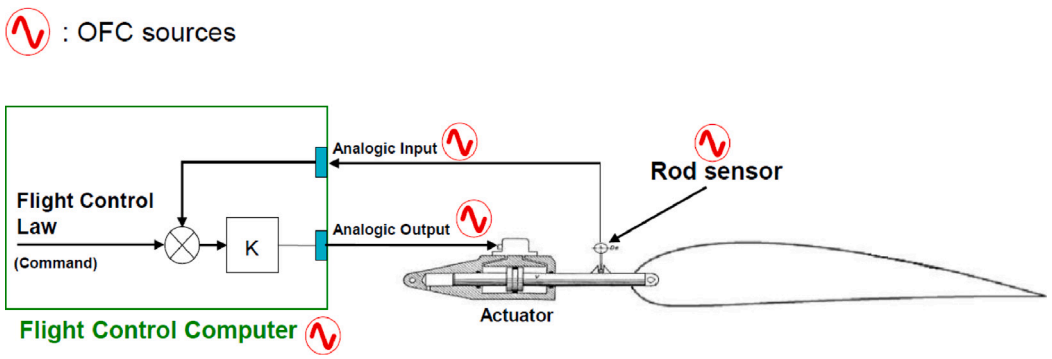

Fig. 1. Control surface control loop and OFC sources.

(2012) used an H_∞ observer for OFC detection on new generation Electro-Hydraulic Actuators. Sun, Patton, and Goupil (2012) proposed a linear time-invariant model based robust fast adaptive fault estimator with unknown input decoupling for oscillatory fault detection. Alwi and Edwards (2013) used an adaptive sliding mode differentiator to reconstruct OFC signals for the purpose of detection. More recently, Goupil, Urbano, and Tourneret (2016) and Urbano, Chaumette, Goupil, and Tourneret (2017) developed and industrially tested a pure data-driven approach for OFC detection based on similarity index computation.

One way to improve a model-based approach for OFC detection is to enhance the residual evaluation step. Varga and Ossmann (2014) used the Narendra criteria (Narendra & Balakrishnan, 1997) as an adaptive way to evaluate the residual using a forgetting factor, as opposed to fixed thresholding of the residual. Trinh, Marx, Goupil, and Ragot (2014) performed a quantitative analysis of a bank of residuals through a correlation test. Lavigne, Cazaurang, Fadiga, and Goupil (2014) investigated the Wald test to distinguish between the fault-free and the faulty case by exploiting the different statistical nature of the residual in both cases.

All of the aforementioned works generally concern a classical hydraulic actuator. Some research has also been performed on OFCs in new generations of actuators such as Electro-Hydraulic Actuators (Sachs, Carl, & Thielecke, 2007). Oscillatory behaviour detection for other kinds of systems can also be found in academic literature. For example, Loutridis (2004) investigated damage detection in gear systems using empirical model decomposition.

In general, an open challenge in the detection of OFC is the design of methods with theoretical guarantees on detectability. Only the availability of such guarantees would win the trust of designers and lead to removing additional structural reinforcements from aircraft design, thus unlocking the potential benefits in terms of fuel efficiency, mass reduction and ease of installation. An important line of development along this direction has been dedicated to unknown input observer (UIO) (Frank & Ding, 1997; Mohammadi, Marquez, & Tavakoli, 2017) and sliding mode observer (SMO) (Edwards, Spurgeon, & Patton, 2000; Mahrukh & Liaqat, 2018; Spurgeon, 2008; Utkin, 1977; Yutian et al., 2010) based fault estimation and detection methods. In this paper, a novel SMO-based OFC detection method will be presented, whose distinctive trait will be the availability of the aforementioned theoretical guarantees, together with a competitive computational complexity.

Contributions & paper outline

An aerospace industrial benchmark dedicated to fault detection in the Flight Control System (FCS) of a civil commercial aircraft was developed by Airbus and Stellenbosch University, South Africa. Detection of OFCs within this industrial benchmark was posed as one of three competitions organized in the context of the 2020 IFAC World Congress. Such competitions are organized in order to enhance industry participation in IFAC events and to bridge the gap with Academia. Furthermore, it gives the opportunity for participants to compete against other international teams. This paper details the solution proposed by the winning team from Delft University of Technology which was selected among all submitted contributions. Two kinds of criteria were applied by the organizers for the final selection and ranking: academic relevance and industrial applicability.

The contribution of this paper is the application of a novel Sliding Mode Observer (SMO) based fault detection scheme to the problem of fast and reliable detection of OFCs in commercial aircraft. We provide theoretical proofs of robustness against false detection, and conditions for guaranteed detectability of OFCs. The detection performance and robustness of the detection scheme are attested by comparison to a state-of-the-art scheme through extensive Monte-Carlo simulations on an industrial benchmark developed by Airbus and Stellenbosch University. Furthermore, the robustness results obtained in theory and simulation are validated by applying the detection scheme to two hours of healthy flight test data provided by Airbus.

The rest of this paper is organized as follows: Section 2 formulates the problem, and models the system and considered OFCs. Section 3 presents the proposed Sliding Mode Observer based fault detection scheme. Section 4 provides the theoretical guarantees on robustness and guaranteed detectability. Section 5 describes the industrial benchmark and the Monte Carlo simulations performed on it to extensively test the OFC detection scheme, and then presents and analyses the simulation results. Section 6 describes the validation of the OFC detection scheme based on experimental flight-test data. Finally, Section 7 summarizes the key findings and presents some promising avenues for future research.

2. Problem formulation and modelling

The problem addressed in this paper is the design of an SMO-based fault detection scheme to detect OFCs in the FCS of a civil commercial aircraft. An OFC is a malfunction that creates a spurious sinusoidal signal which propagates through the flight control loop and causes unwanted oscillations of a control surface. These OFCs are primarily caused by electrical components that suddenly enter a fault-mode where an oscillatory signal is generated. A diagram of the typical actuator control loop, with potential OFC sources, is shown in Fig. 1.

The OFC signal may originate at a number of sources, as indicated on the diagram. For this paper we consider OFCs that originate at either the servo current input commanded by the flight control computer or at the rod position sensor. Laboratory tests performed by Airbus concluded that OFC signals resemble sinusoidal signals with a fixed but unknown frequency which is uniformly distributed in a bounded frequency range. Beyond such frequency range, the OFC has no significant effects because of the low-pass behaviour of the actuator. Furthermore, OFCs can occur as *liquid* and *solid* faults. Liquid faults are additive, where an oscillatory signal is superimposed on the existing signals in the control loop, and the actuator can still respond to reference commands. Solid failures completely replace the existing signals in the

control loop, causing the flight control computer to no longer have any control over the actuator.

The objective of the fault detection scheme is to detect the OFC within a specified maximum number of oscillation periods, whatever the frequency. Since the detection time is expressed as a number of oscillation periods, the time that is allowed for detection will depend on the specific OFC frequency. This objective is chosen as it relates to the aircraft structural design. Any OFCs not detected within this time cause additional structural loads and should thus be considered in the structural design. The specific number of oscillations that is allowed before the structural loads occur depends on many factors, such as type of control surface and the aircraft model and is generally obtained through exhaustive structural load and stress simulations.

The detection scheme should detect OFCs with amplitudes as small as possible. However, it must not produce false alarms during normal flight in various atmospheric conditions. The detection scheme must be able to detect both liquid and solid failures, and must be able to detect OFC signals that originate at either the servo current input or at the rod position sensor.

A model-based fault detection approach is used in this work, utilizing analytical redundancy by comparing the measured behaviour of the actuators with the expected fault-free behaviour, which is obtained by simulating the motion of a fault-free actuator in parallel with the real actuator. This is however done without using explicitly the state estimation error, distinguishing the proposed method from other model-based approaches such as interval observer based or set based approaches. The main advantages of the detection method proposed in this work are its strong guarantees on robustness and detectability, and competitive computational cost.

Remark 1. The use of a model-based detection approach instead of spectral methods for detection of oscillatory faults might be questioned. However, in order to effectively use spectral methods, multiple FFTs need to be calculated in real-time, which is infeasible with the limited available computational resources. The detection approach proposed in this paper only requires 120 scalar operations to be performed per evaluation.

The mathematical models for the real servo actuator, the oscillatory failure, and the analytically redundant servo model are described in the following subsections.

2.1. Real servo model

The real aircraft servo is modelled in the industrial benchmark as

$$\begin{aligned} \dot{p} &= V_c \sqrt{\frac{\Delta P + \frac{\delta k_{aero}\mathrm{sgn}(V_c)}{S}}{\Delta P_{ref} + \frac{k_d V_c^2}{S}}} + \Gamma, \\ V_c &= k_c(K(p_{\mathrm{ref}} - p_{\mathrm{meas}}) + i_f), \\ \delta &= k_p(p), \quad p_{\mathrm{ref}} = k_\delta(\delta_{\mathrm{des}}), \\ \delta_{\mathrm{meas}} &= \delta + \xi_\delta, \quad p_{\mathrm{meas}} = p + \xi_p + p_f, \end{aligned} \tag{1}$$

where p is the servo rod position in [mm], δ is the control surface deflection in [deg], and V_c is the commanded voltage to the servo. p_{ref} and p_{meas} are the desired and measured servo rod position in [mm], which are only used in the internal servo control loop. δ_{des} and δ_{meas} are the desired and measured control surface deflections in [deg], which are the only input and output of the system, respectively. ξ_p and ξ_δ are the measurement noises for the rod position and control surface deflection sensors, respectively.

Furthermore, ΔP_{ref}, S, and K are known parameters. ΔP, k_d, and k_{aero} are unknown parameters. Γ represents unmodelled, but bounded, behaviour of the real servo. Γ is defined in Table 1 based on p_{ref}. k_p and k_δ are non-increasing known functions and k_c is a non-decreasing known function, all of which are defined as lookup tables. Lastly, p_f and i_f are the faults that can occur in servo rod position measurement and the commanded current respectively. All model parameters can be found in Table 1.

Table 1
Actuator model parameters.

Parameter	Value [Unit]	Parameter	Range [Unit]
ΔP_{ref}	21 [N/mm^2]	ΔP	[15, 29] [N/mm^2]
K	0.4 [mA/mm]	k_d	[3, 6.2] [N s^2/mm^2]
S	5000 [mm^2]	k_{aero}	[435, 975] [N/deg]
		Γ	$[-0.07, 0.07]\frac{\mathrm{d}^2 p_{\mathrm{ref}}}{\mathrm{d}t^2}$ [mm/s^2]

The servo in healthy conditions can be modelled as

$$\begin{aligned} \dot{p}^0 &= V_c^0 \sqrt{\frac{\Delta P + \frac{\delta k_{aero}\mathrm{sgn}(V_c^0)}{S}}{\Delta P_{ref} + \frac{k_d V_c^{0\,2}}{S}}} + \Gamma, \\ V_c^0 &= k_c(K(p_{\mathrm{ref}} - p^0_{\mathrm{meas}})), p^0_{\mathrm{meas}} = p^0 + \xi_p, \end{aligned} \tag{2}$$

where superscript ^{0} denotes the healthy condition.

Assumption 1. The unknown parameters ΔP, k_d, and k_{aero} can be expressed as the summation of known nominal values, ΔP_N, k_{d_N} and k_{aero_N}, and unknown variations $\Delta\tilde{P}$, $\tilde{k}_d$ and $\tilde{k}_{\mathrm{aero}}$ with known bounds. Furthermore, the unmodelled dynamics Γ is bounded as $|\Gamma| \leq \gamma$.

Assumption 2. The sensor noises ξ_p and ξ_δ are zero-mean and can be bounded for all time as $|\xi_p| \leq \bar{\xi}_p$ and $|\xi_\delta| \leq \bar{\xi}_\delta$, respectively.

Assumption 3. The faults p_f and i_f can be bounded for all time as $|p_f| \leq \bar{p}_f$ and $|i_f| \leq \bar{i}_f$, respectively.

Assumption 4. A fault occurs at time T_f, such that we have the healthy case where $p_f(t) = 0$ and $i_f(t) = 0$ for $t < T_f$ and a faulty case afterwards.

2.2. Fault modes

The faults considered are oscillatory faults introduced either in the commanded current, i_f, or in the rod position sensor, p_f. These faults can, as previously explained, occur in solid and liquid form, which are denoted as

$$\text{Liquid:} \begin{cases} p_f &= p_f^{\mathrm{osc}} \\ i_f &= i_f^{\mathrm{osc}} \end{cases}$$

$$\text{Solid:} \begin{cases} p_f &= p_{\mathrm{ref}} - p^0_{\mathrm{meas}} + p_f^{\mathrm{osc}} \\ i_f &= -K(p_{\mathrm{ref}} - p^0_{\mathrm{meas}}) + i_f^{\mathrm{osc}} \end{cases}$$

where p_f^{osc} and i_f^{osc} are sinusoidal with an unknown constant frequency of $1 - 10$ [Hz], and an unknown fixed amplitude. In practice, both these faults rarely occur, therefore it is justified to make the following assumption.

Assumption 5. The faults in the commanded current and rod position measurement never occur simultaneously.

2.3. Detector servo model

The detector only has access to the nominal parameters and δ_{des} and δ_{meas}, i.e. the input and output of the system. Therefore model (2) cannot be implemented directly. Based on the known variables and nominal parameters and functions, the servo can be modelled by the detector as

$$\begin{aligned} \dot{p}_{\mathrm{model}} &= \hat{V}_c \sqrt{\frac{\Delta P_N}{\Delta P_{ref} + \frac{k_{d_N}\hat{V}_c^2}{S}}}, \\ \hat{V}_c &= k_c(K(k_\delta(\delta_{\mathrm{des}}) - k_p^{-1}(\delta_{\mathrm{meas}}))), \end{aligned} \tag{3}$$

where the used nominal model parameters are design parameters of the detector. Here $k_p^{-1}(\cdot)$ is the inverse function of $k_p(\cdot)$ such that $k_p^{-1}(\delta_{\text{meas}})$ is an approximation of p_{meas}. One can see that by the use of $k_p^{-1}(\delta_{\text{meas}})$ as an approximation of p_{meas}, the dynamics of p_{model} has no internal state and has become a direct function of only δ_{des} and δ_{meas}.

Remark 2. Note that faults i_f and p_f are indistinguishable based on the signals available to the detector, i.e. δ_{des} and δ_{meas}. Therefore, in theory a composite fault $i_f - Kp_f$ could be considered in the same way as the individual faults.

3. Sliding mode observer based fault detection scheme

In this section the novel sliding mode observer (SMO) based fault detection scheme will be presented. Theoretical guarantees for robustness and guaranteed detectability are presented in Section 4. The theoretical guarantee on robustness is especially useful for the detection of OFCs, as such faults only rarely occur.

The scheme relies on known bounds on the state estimation error of the SMO, which are guaranteed to hold under healthy conditions. Therefore, once the observer error is no longer within these bounds, this is guaranteed to be caused by a fault. Note that due to the inherent invariance properties of SMOs the state estimation error will never deviate from a bounded region around the origin. Instead, the bounds are designed such that when a fault occurs, one of the bounds will deviate from zero. To detect such occurrence without knowing the true estimation error, the known bounds on the estimation error are compared directly leading to detection when the lower bound becomes larger than the upper bound or vice versa.

First, to aid the implementation of the detection scheme, we will write the relation between $\dot{p}$, Eq. (1), and $\dot{p}_{\text{model}}$, Eq. (3), as

$$\dot{p} = \dot{p}_{\text{model}} + \Theta + F,$$

where $F \triangleq \dot{p} - \dot{p}^0$ is the effect of the fault and $\Theta \triangleq \dot{p}^0 - \dot{p}_{\text{model}}$ includes the effects of unmodelled dynamics, parameter uncertainty, and measurement noise. Note that by Assumption 4 we have $F(t) = 0\ \forall t < T_f$. The combined uncertainty Θ can be bounded as $|\Theta| \leq \theta$ where

$$\theta = \max_{\tilde{k}_d, \Delta\tilde{P}, \tilde{k}_{\text{aero}}, \Gamma, \xi_\delta, \xi_p} (|\dot{p}^0 - \dot{p}_{\text{model}}|)\,. \tag{4}$$

An explicit form of θ based on the actuator dynamics in Eq. (2) is derived in Appendix A. Note that there are more ways to obtain a bound θ, however, it is beneficial to the performance of the detector that θ is as small as possible. With this bound and Assumption 1, the dynamics of the real servo can be bounded as

$$\dot{p}_{\text{model}} - \theta + F \leq \dot{p} \leq \dot{p}_{\text{model}} + \theta + F$$

where θ can be calculated based exclusively on quantities known to the detector.

3.1. Sliding mode observer

The fault detection scheme is based on the error dynamics of a Sliding Mode Observer (SMO). The SMO estimates the servo rod position using

$$\dot{\hat{p}} = \dot{p}_{\text{model}} - K_L e_{\text{meas}} + \nu \tag{5}$$

where $K_L < 0$ is the linear observer gain, the switching term ν is defined as

$$\nu = K_s \text{sgn}(e_{\text{meas}}),$$

where K_s is the switching gain, and $e_{\text{meas}} = k_p^{-1}(\delta_{\text{meas}}) - \hat{p}$ is the measured observer error. K_s is set to $K_s = \theta + \eta$. Here η is a positive constant, such that K_s is an upper bound on the model uncertainty.

By defining $e = p - \hat{p}$, the observer error dynamics can be obtained using Eqs. (1) and (5) as

$$\dot{e} = \Theta + F + K_L e_{\text{meas}} - \nu\,. \tag{6}$$

Note here that e_{meas} relates to e as $e_{\text{meas}} = e + k_p^{-1}(\delta_{\text{meas}}) - p$. This relation is such that if $\delta_{\text{meas}} = \delta$, we have $e_{\text{meas}} = e$. This relation is used below in Theorem 1.1 to prove that in the healthy case e converges to a bounded region around the origin.

Theorem 1. *The initial rod position estimate $\hat{p}(0)$ can always be chosen such that the observer error dynamics in Eq. (6) satisfies the following propositions:*

1. *$\underline{e}^0 \leq e(t) \leq \bar{e}^0$ and $\underline{\dot{e}}^0 \leq |\dot{e}(t)| \leq \bar{\dot{e}}^0$ for $t < T_f$, i.e. in the healthy case,*
2. *$sgn(\dot{e}(t)) = -sgn(e_{meas}(t))$ for $t < T_f$, i.e. in the healthy case,*
3. *$\underline{\dot{e}}^+ \leq \dot{e} \leq \bar{\dot{e}}^+$ if $e_{meas} > 0$ and $\underline{\dot{e}}^- \leq \dot{e} \leq \bar{\dot{e}}^-$ if $e_{meas} < 0$,*

where

$$\underline{e}^0 = \min_{p,\xi_\delta}(p - k_p^{-1}(k_p(p) + \xi_\delta))$$
$$\bar{e}^0 = \max_{p,\xi_\delta}(p - k_p^{-1}(k_p(p) + \xi_\delta))$$
$$\bar{\dot{e}}^+ = K_L e_{meas} - \eta + F$$
$$\underline{\dot{e}}^+ = -2\theta + K_L e_{meas} - \eta + F$$
$$\bar{\dot{e}}^- = 2\theta + K_L e_{meas} + \eta + F$$
$$\underline{\dot{e}}^- = K_L e_{meas} + \eta + F$$
$$\underline{\dot{e}}^0 = |K_L e_{meas}| + \eta$$
$$\bar{\dot{e}}^0 = 2\theta + |K_L e_{meas}| + \eta$$

Furthermore, the healthy bounds $\underline{\dot{e}}^0$, $\bar{\dot{e}}^0$, $\underline{e}^0$, and $\bar{e}^0$ depend only on known parameters and variables.

Proof. For readability, the proof is presented in Appendix B □

Corollary 1. *From Theorem 1 it follows that $e_{meas} + \underline{e}^0 \leq e \leq e_{meas} + \bar{e}^0$*

Proof. By definition $e - e_{\text{meas}} = p - k_p^{-1}(\delta_{\text{meas}}) = p - k_p^{-1}(k_p(p) + \xi_\delta)$. Therefore, by definition of $\underline{e}^0$ and $\bar{e}^0$ in proposition 1 of Theorem 1 we have $\underline{e}^0 \leq e - e_{\text{meas}} \leq \bar{e}^0$, which is equivalent to the corollary statement. □

3.2. Observer error bounds

Based on the bounds on the healthy behaviour from Theorem 1, and the real behaviour represented by e_{meas}, time-varying upper and lower bounds on e are constructed which are guaranteed to hold under healthy behaviour. These bounds will be denoted by $\underline{e}$ and $\bar{e}$ for the lower and upper bound respectively.

Let us denote the times at which new measurements from the continuous time system (1) become available to the observer as $\{t_m\}$, as visualized in Fig. 2. Then, at each t_m, e can be bounded using Corollary 1 as $e_{\text{meas}} + \underline{e}^0 \leq e \leq e_{\text{meas}} + \bar{e}^0$. Combining this with the bounds on e from Theorem 1, we obtain some static bounds on the healthy e as

$$\max(e_{\text{meas}} + \underline{e}^0, \underline{e}^0) \leq e \leq \min(e_{\text{meas}} + \bar{e}^0, \bar{e}^0) \tag{7}$$

Based on the bounds on the healthy $\dot{e}$ from Theorem 1.1 and 1.2 also time-varying bounds on the healthy e can be defined as

$$\begin{aligned} &\text{If } e_{\text{meas}}(t_{m-1}) < 0 \\ &\int_{t_{m-1}}^{t_m} \underline{\dot{e}}^0(T)\mathrm{d}T \leq e(t_m) - e(t_{m-1}) \leq \int_{t_{m-1}}^{t_m} \bar{\dot{e}}^0(T)\mathrm{d}T \\ &\text{If } e_{\text{meas}}(t_{m-1}) > 0 \\ &-\int_{t_{m-1}}^{t_m} \bar{\dot{e}}^0(T)\mathrm{d}T \leq e(t_m) - e(t_{m-1}) \leq -\int_{t_{m-1}}^{t_m} \underline{\dot{e}}^0(T)\mathrm{d}T \end{aligned} \tag{8}$$

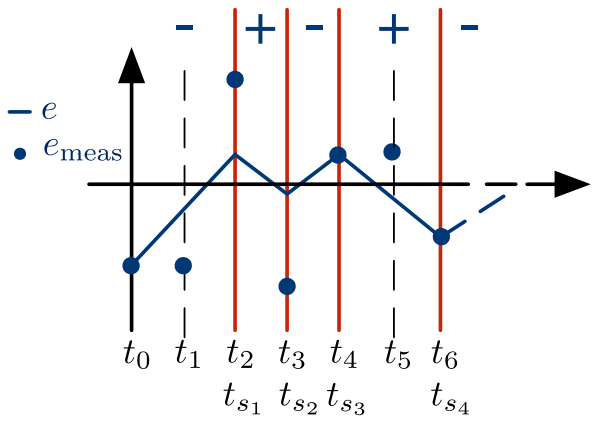

Fig. 2. Nominal behaviour of observer error e, where t_m for $m \in \{0 \dots 6\}$ denote the measurement times and t_{s_i} for $i \in \{1 \dots 4\}$ denote the switching times.

Then, by combining the bound of Eqs. (7) and (8) we obtain definitions of $\tilde{e}$ and $\underline{e}$ as

$$\begin{aligned}
&\text{If } e_{\text{meas}}(t_{m-1}) < 0 \\
&\quad \tilde{e}(t_m) = \min\Big(\int_{t_{m-1}}^{t_m} \dot{\tilde{e}}^0(T)\mathrm{d}T, e_{\text{meas}}(t_m) + \tilde{e}^0, \tilde{e}^0\Big) \\
&\quad \underline{e}(t_m) = \max\Big(\int_{t_{m-1}}^{t_m} \dot{\underline{e}}^0(T)\mathrm{d}T, e_{\text{meas}}(t_m) + \underline{e}^0, \underline{e}^0\Big) \\
&\text{If } e_{\text{meas}}(t_{m-1}) > 0 \\
&\quad \tilde{e}(t_m) = \min\Big(-\int_{t_{m-1}}^{t_m} \dot{\underline{e}}^0(T)\mathrm{d}T, e_{\text{meas}}(t_m) + \tilde{e}^0, \tilde{e}^0\Big) \\
&\quad \underline{e}(t_m) = \max\Big(-\int_{t_{m-1}}^{t_m} \dot{\tilde{e}}^0(T)\mathrm{d}T, e_{\text{meas}}(t_m) + \underline{e}^0, \underline{e}^0\Big)
\end{aligned} \tag{9}$$

where by design $\underline{e} \le e(t) \le \tilde{e}$ if $F(\tau) = 0 \forall \tau < t$.

Remark 3. Three bounds on the healthy e are derived in Theorem 1, Corollary 1 and Eq. (8).[1] Each of these bounds is proven to always bound the healthy e. Therefore, a less conservative bound on the healthy e can be obtained by combining the individual bounds as $\max(*) = \underline{e} \le e \le \tilde{e} = \min(*)$ which is still guaranteed to always bound the healthy e. A formal proof of the robustness of $\tilde{e}$ and $\underline{e}$ is provided in Theorem 2.

Remark 4. In the edge case where $e_{\text{meas}}(t_{m-1}) = 0$, we consider $e_{\text{meas}}(t_{m-1}) = -e_{\text{meas}}(t_{m-2})$ in determining which case to use in Eq. (9). Furthermore $\tilde{e}(t_0)$ and $\underline{e}(t_0)$ are fully defined by the static bounds in Eq. (7).

3.3. Fault detection logic

Ideally, one would like to directly use these bounds as thresholds on e to detect faults, i.e. a fault is detected if $\underline{e} \le e \le \tilde{e}$ is violated. However, this is not possible because only e_{meas} is known to the detector, and not e itself. Therefore, instead, the bounds are compared to each other for detection such that a fault is detected if

$$\underline{e}(t_m) > \tilde{e}(t_m) \tag{10}$$

is satisfied. This detection condition can be monitored at any t_m.

Remark 5. The SMO based fault detection method proposed in this paper is distinctly different from traditional fault detection methods such as set based methods or those based on interval observers. These methods derive detectability from having a sufficiently large state estimation error. The method presented here, however, does not require the state estimation error to increase. Instead the detection condition in Eq. (10) only depends on two bounds, which will become conflicting for sufficiently large faults. Furthermore, the inherent capability of the SMO to simultaneously estimate the state and fault has the potential to be used in future work on identification and accommodation of the fault.

[1] The bounds defined in (8) are proven to hold by Theorem 1.1 and 1.2

4. Theoretical analysis of robustness and detectability

In this section robustness and detectability guarantees of the proposed detection method are presented. To this end we need to define $\{t_{s_i}\}$ as the times at which e_{meas} changes sign. This is visualized in Fig. 2. Using this notation, first it will be proven that it is guaranteed that there is no false detection. Then sufficient conditions on the fault will be presented for which detection is guaranteed. The detectability proof is split into two parts. Firstly in Lemma 1 it is proven that some conditions on $\dot{e}$ allow us to guarantee detection within a specified time. Then in Theorem 3 it is shown that the conditions in Lemma 1 can be achieved by sufficiently large faults. Furthermore, note that both Lemma 1 and Theorem 3 contain two conditions which address positive and negative faults respectively.

To increase readability the proofs of Theorem 2 and Lemma 1 are presented in Appendices C and D respectively.

Theorem 2 (*Robustness*). *In healthy conditions, i.e. for $t < T_f$, the detection criterion (10) will not be satisfied at time t.*

Lemma 1 (*Detectability*). *If*

$$\dot{\underline{e}}^0 > -\dot{e}^+_{i+j} + \epsilon^+ \text{ and } \dot{\tilde{e}}^0 < \dot{e}^-_{i+j} - \epsilon^+ \text{ for the period } \left[t_{s_{2i}}\ t_{s_{2i+2N}}\right] \text{ with } \epsilon^+ > 0.$$

Then, detection is guaranteed to occur before $t_{s_{2i+2N}}$ if

$$\sum_{j=0}^{N-1} t^+_{i+j} > \frac{2(\tilde{e}^0 - \underline{e}^0 - |e_{meas}|)}{\phi(\dot{\underline{e}}^0 + \dot{\tilde{e}}^0)\epsilon^+}$$

where $\phi \le \frac{1}{\dot{e}^-_{i+j}}$ $\forall i, j$. Likewise if

$$\dot{\tilde{e}}^0 < -\dot{e}^+_{i+j} - \epsilon^- \text{ and } \dot{\underline{e}}^0 > \dot{e}^-_{i+j} + \epsilon^- \text{ for the period } \left[t_{s_{2i}}\ t_{s_{2i+2N}}\right] \text{ with } \epsilon^- > 0.$$

Then, detection is guaranteed to occur before $t_{s_{2i+2N}}$ if

$$\sum_{j=0}^{N-1} t^+_{i+j} > \frac{2(\tilde{e}^0 - \underline{e}^0 - |e_{meas}|)}{\phi(\dot{\underline{e}}^0 + \dot{\tilde{e}}^0)\epsilon^-}$$

where $\phi \le \frac{1}{\dot{e}^-_{i+j}}$ $\forall i, j$.

Theorem 3 (*Detectability*). *There exist a τ such that the detection Condition (10) is guaranteed to be satisfied if $F > \tilde{e}^0 - \underline{e}^0 + \epsilon^+$ or $F < \underline{e}^0 - \tilde{e}^0 - \epsilon^-$ for a duration longer than τ.*

Proof. In Lemma 1 conditions on $\dot{e}^+$ and $\dot{e}^-$ are presented such that detection occurs within a duration $\tau = t_{s_{2i+2N}} - t_{s_{2i}}$. Here N is implicitly defined in Lemma 1. In this proof it thus remains to be shown that the conditions on $\dot{e}^+_{i+j}$ and $\dot{e}^-_{i+j}$ from Lemma 1 hold for any fault $F > \tilde{e}^0 - \underline{e}^0 + \epsilon^+$ or $F < \underline{e}^0 - \tilde{e}^0 - \epsilon^-$.

If $F > \tilde{e}^0 - \underline{e}^0 + \epsilon^+$, using the bounds from Theorem 1, we can write

$$\begin{aligned}
\dot{\underline{e}}^+ &= -\dot{\tilde{e}}^0 + F > -\dot{\tilde{e}}^0 + \dot{\tilde{e}}^0 - \dot{\underline{e}}^0 + \epsilon^+ = -\dot{\underline{e}}^0 + \epsilon^+, \\
\dot{\underline{e}}^- &= \dot{\underline{e}}^0 + F > \dot{\underline{e}}^0 + \dot{\tilde{e}}^0 - \dot{\underline{e}}^0 + \epsilon^+ = \dot{\tilde{e}}^0 + \epsilon^+,
\end{aligned}$$

Similarly if $F < \underline{e}^0 - \tilde{e}^0 - \epsilon^-$, we can write

$$\dot{\tilde{e}}^+ < -\dot{\tilde{e}}^0 - \epsilon^- \quad \text{and} \quad \dot{\tilde{e}}^- < \dot{\underline{e}}^0 - \epsilon^-$$

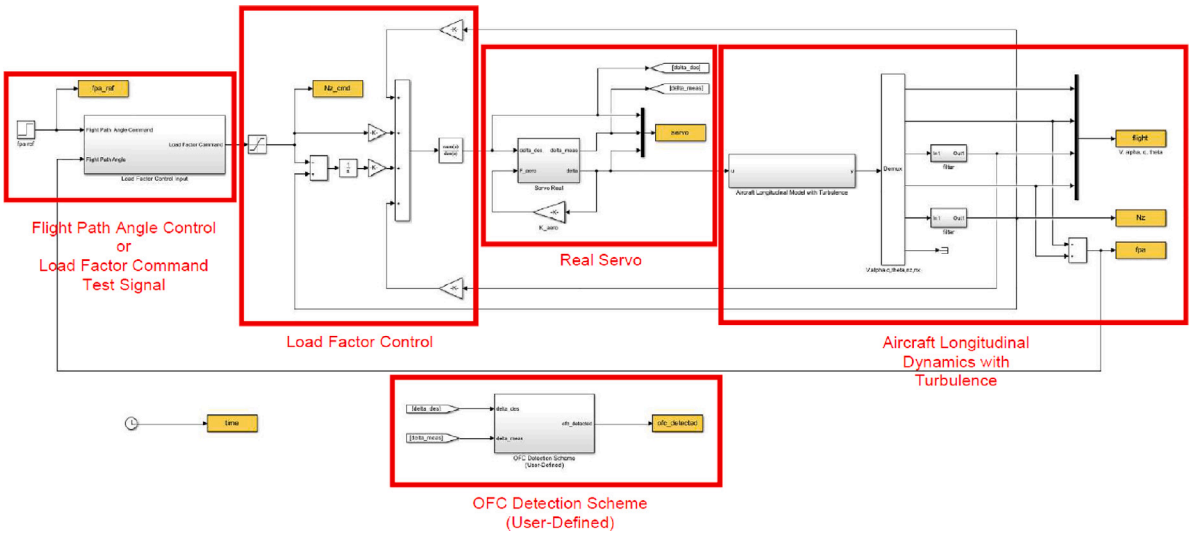

Fig. 3. Simulink Model for OFC Benchmark.

This proves that the conditions on F presented in this theorem are sufficient conditions for the conditions on $\dot{e}^{+}_{i+j}$ and $\dot{e}^{-}_{i+j}$ from Lemma 1, and thus also sufficient conditions for detection. □

Remark 6. From the analysis in this section it can be seen that robustness of the detector is guaranteed. Therefore, there is no trade-off between robustness and detectability as is common in fault detection literature. In Lemma 1 and Theorem 3 one can however see that the fault magnitude and time required for detection are dependent on the bounds on the observer error dynamics e as presented in Theorem 1. Therefore, detectability can be influenced by the design parameters of the observer.

5. Simulation study

In this section, the robustness and detection performance of the proposed OFC detection scheme is demonstrated through exhaustive Monte Carlo simulations within the industrial benchmark for OFC detection developed by Airbus and Stellenbosch University. To this end, first the benchmark simulation will be introduced, followed by the analysis of results obtained through Monte Carlo simulations.

5.1. Industrial OFC benchmark

The OFC detection scheme was tested in simulation using a Simulink model that was developed by Airbus and Stellenbosch University for the Aerospace Industrial Benchmark on Fault Detection competition at the 21st IFAC World Congress. The Simulink model is a high-fidelity model of a control loop for a specific flight phase, namely the cruise phase, and for a given flight point. It allows for generating the control surface position corresponding to a given flight path angle or load factor command. It also allows the injection of OFCs originating from the rod position measurement or the current commanded by the FCC, at different frequencies and for a given amplitude. A top-level diagram of the Simulink model is shown in Fig. 3.

The Simulink model consists of the following functional blocks: The real servo actuator with the option to inject an OFC, the aircraft longitudinal dynamics with turbulence, the load factor controller, the flight path angle controller, and the OFC detection scheme.

The real servo actuator block implements the model in Eq. (1) that describes the motion of the servo actuator in response to a control surface deflection command, and also allows an OFC to be injected. The aircraft longitudinal dynamics block models the longitudinal motion of the aircraft in response to the elevator control surface deflection, including the effect of external wind turbulence. The wind turbulence is modelled using a Von Karman Wind Turbulence Model from the Simulink Aerospace Blockset. The load factor controller block controls the load factor of the aircraft by commanding the elevator control surface deflection using the measured load factor and measured pitch rate of the aircraft as feedback. The flight path angle controller block controls the flight path angle of the aircraft to maintain level flight by commanding the load factor using the measured flight path angle as feedback. The OFC detection scheme block implements the SMO-based approach described in Section 3.

Table 2
Observer gains and nominal model parameters.

Parameter	Value [Unit]	Parameter	Value [Unit]
η	0.1 [−]	ΔP_N	28 [N/mm^2]
K_L	−1 [s^{-1}]	k_{d_N}	5.5 [n s^2/mm^2]
γ	$\lvert 0.07 \frac{d^2 P_{ref}}{dt^2} \rvert$	k_{aero_N}	650 [N/deg]

5.2. Detector performance analysis through Monte Carlo simulation

Extensive Monte Carlo simulations were performed using this benchmark model and the parameters in Table 1. Furthermore, the observer gains have been chosen as in Table 2. The nominal model parameters and their uncertainties have been identified based on extensive flight test data from the considered actuator. Note that the nominal model parameters are not in the middle of their respective uncertainty ranges. Instead, they are chosen as the expected value of the probability distribution over the uncertainty range. Furthermore, the detection performance is not very sensitive to observer gains η and K_L. However, in general higher gains provide faster detection, at the cost of increasing the minimum fault magnitude that can be detected.

Simulations have been performed while injecting faults in the commanded current and rod position sensor as described in Section 2.2. Detection performance is shown for the full range of considered fault frequencies, amplitudes, and fault types.

The results of the Monte Carlo simulations are shown in Figs. 4 and 6 for all considered fault types. These results are obtained by performing 200 simulations for each combination of fault frequency

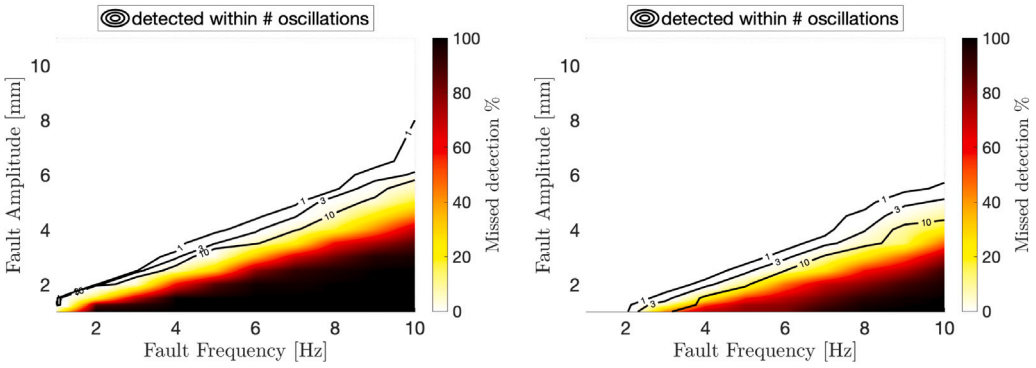

(a) Liquid fault in rod position sensor (b) Solid fault in rod position sensor

Fig. 4. Performance of the presented SMO-based detection method for detection of faults in the rod position sensor.

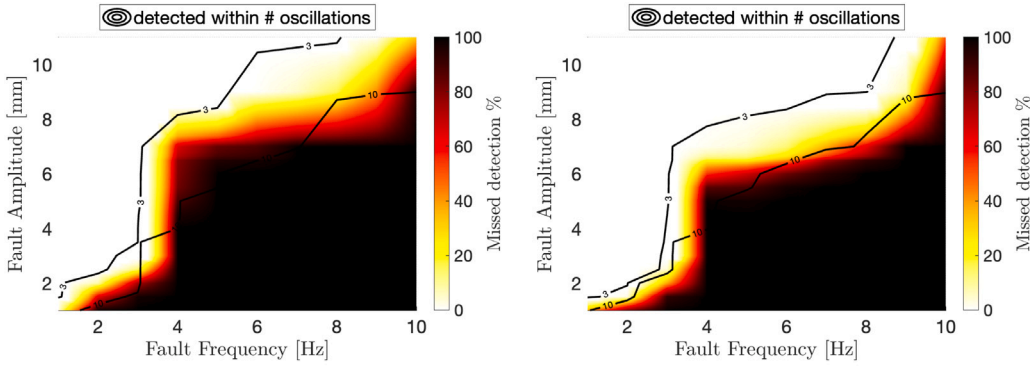

(a) Liquid fault in rod position sensor (b) Solid fault in rod position sensor

Fig. 5. Performance of the detection method from Goupil (2010) for detection of faults in the rod position sensor.

and amplitude, with different uncertainties. For each simulation instance the uncertain parameters ΔP, k_d, k_{aero}, and Γ are drawn from a uniform distribution within the possible set defined in Assumption 1. Furthermore, excitation of the system is obtained through p_{ref}, which is calculated by using the load factor control in flight path mode performing a stabilization task under four different turbulence conditions.

Recall that the objective of the detection scheme is to detect an OFC within a specified maximum number of oscillations, while having no false detection. This detection objective derives from the additional loads caused by the OFC if it remains unmitigated for more than this number of oscillations. The specific number of oscillations that is allowed before the structural loads occur depends on many factors, such as the type of control surface and the aircraft model. To show the broad applicability of the method, in Figs. 4 and 6 the contours show the regions for which detection always occurs within 1, 3, and 10 oscillations. Furthermore, the background colour shows the percentage of *missed detections*, which is defined as no detection within 3 oscillations of the fault. Note that the choice to show results for detection within 1, 3, and 10 oscillations has been made as an example as they span a realistic range of potential detection requirements, but they do not reflect the actual requirement for the considered actuator.

From the contours in Figs. 4 and 6 it can be seen that for all fault types, faults with a sufficiently large amplitude can be consistently detected within any specified maximum number of oscillations. This shows that the detection objective can be achieved for all fault types and frequencies. Furthermore, during the 96,000 simulations performed to obtain the Monte Carlo results, no false alarms were recorded, demonstrating the robustness of the detection scheme.

Furthermore, it can be seen that the fault amplitude required for consistent detection increases approximately linearly with fault frequency. This finding is supported by theory through Theorem 3, where it is proven that detection is guaranteed for sufficiently positive (or negative) faults which persist longer than τ. For the considered zero-mean liquid faults, this means detection guarantees for higher frequency faults demand a larger amplitude. Lastly, it can be seen that the detector consistently shows better detection performance for solid faults than for liquid faults. Unlike liquid faults, solid faults are not zero-mean. Therefore, we can once again invoke Theorem 3 to explain the improved detection performance. The nonzero mean of the solid fault will always cause an increase in either the duration for which the oscillatory fault is positive or negative.

To get a feeling for the type of data from which the extensive Monte Carlo results presented above are obtained, Fig. 8 shows simulation results for a single realization of the uncertainty. Here, a liquid fault in the commanded current with frequency 5 Hz and amplitude 1.5 mA is introduced at 10 s under light turbulence conditions. Fig. 8(a) shows the control surface deflection for the performed stabilization maneuver, and the behaviour of the fault detection bounds $\bar{e}$ and $\underline{e}$ is shown in Fig. 8(b). One can see that for this realization of the uncertainty fault detection occurs well within 0.1 [s].

Remark 7. It can be seen in Fig. 8(b) that after the first detection, the detection decision is not maintained continuously. Specifically detection only occurs around the times at which the oscillatory fault peaks. As the presented detector has strong robustness guarantees even a short period of detection is enough to guarantee the presence of a fault, after which the detector latches and the actuator is considered

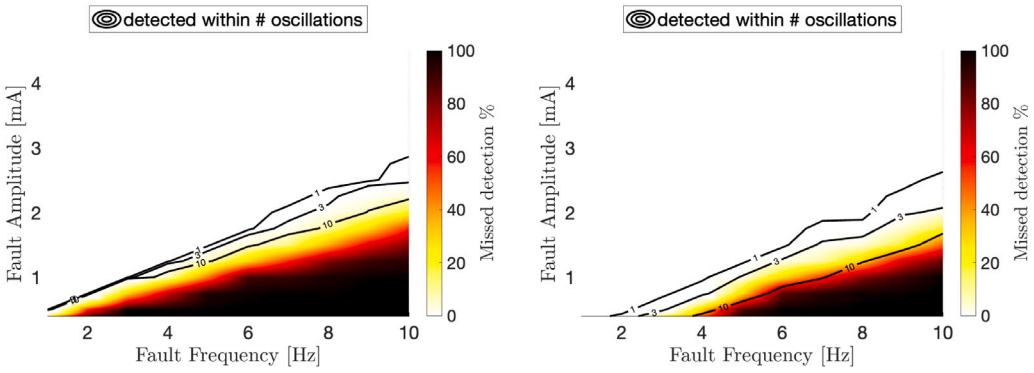

(a) Liquid fault in commanded current (b) Solid fault in commanded current

Fig. 6. Performance of the presented SMO-based detection method for detection of faults in the commanded current.

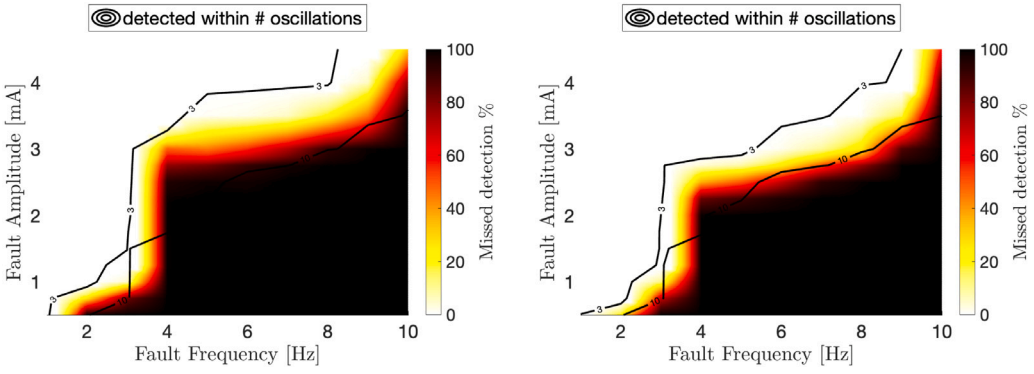

(a) Liquid fault in commanded current (b) Solid fault in commanded current

Fig. 7. Performance of the detection method from Goupil (2010) for detection of faults in the commanded current.

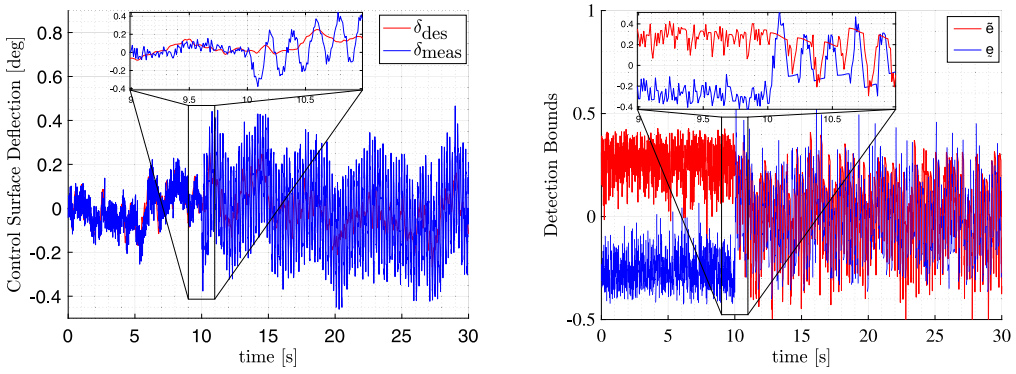

(a) Measured and commanded actuator deflection for a stabilization task under light turbulence.

(b) Fault detection bounds $\bar{e}$ and $\underline{e}$ leading to detection of the fault within one oscillation.

Fig. 8. Example of behaviour of the actuator and fault detector under a fault in the commanded current. A fault with frequency of 5 Hz and amplitude of 1.5 mA occurs at 10 s.

faulty until inspection. Therefore, the time of first detection has been used as performance indicator throughout this section. Furthermore, the regularity of detection at the fault peaks can be used to obtain some continuity in detection. This is, however, outside the scope of this paper.

5.3. Comparison to industrial state of practice

In this section the performance of the proposed SMO-based OFC detector is compared to the current industrial state of practice as published in Goupil (2010). In Goupil (2010) OFCs are detected based on a scheme that is primarily based on *oscillation counting*, i.e. it counts the oscillations of the residual and raises an alarm if sufficient oscillations are counted within a sliding window. This *oscillation counting* OFC detector is currently implemented on the A380.

To make the comparison, Monte Carlo simulations have been performed using the *oscillation counting* OFC detector with the same settings as used in Section 5.2. The obtained results using the *oscillation counting* OFC detector for all fault types can be found in Figs. 5 and 7.

One can see that the OFC amplitude required for detection using the oscillation counting detector sharply increases around a frequency of 3 Hz for all fault types, while it is only slowly increasing over the remainder of the frequency range. This sharp increase is due to the

Table 3
Metrics describing the flight test data and corresponding detection bounds.

Data	Duration	δ_{meas} [deg]		$\tilde{e} - \underset{\sim}{e}$ [mm]		
set	[min]	Variance	Range	Range	Median	< 0
1	63	16.6	$[-35.3, 35.1]$	$[0.11, 0.74]$	0.62	No
2	22	10.6	$[-33.5, 24.3]$	$[0.08, 0.74]$	0.62	No
3	24	23.7	$[-30.6, 26.1]$	$[0.07, 0.74]$	0.62	No

structure of the oscillation counting detector, which uses two detectors for the frequencies above and below 3 Hz. This profile is distinctly different than for the SMO-based detector, where the OFC amplitude required for detection increases linearly. Furthermore, one can see that the oscillation counting scheme cannot detect any fault consistently within 1 oscillation.

Comparing the detection performance, one can see that the OFC amplitude required for sufficiently fast detection with the oscillation counting detector is comparable to the proposed SMO-based detector for frequencies lower than 3 Hz. For frequencies higher than 3 Hz the OFC amplitude required for sufficiently fast detection is two to three times as large as with the proposed SMO-based detector. This means that implementation of the proposed SMO-based detector provides for better detection performance, allowing for the structural design to consider a smaller class OFCs.

6. Experimental study

To bridge the gap between academic research and real practice, measurements of the actuator behaviour have been obtained from flight tests performed by Airbus. These measurements show the healthy behaviour of the actuator in real flight and are utilized here to validate Theorem 2, where it is proven the detection method is free of false alarms. The verification of the robustness is a key step for the industrial acceptance of the developed solution. In particular OFCs are very rare events so the assessment of the probability to degrade the so-called Mean Time Between Failure (MTBF) of flight control equipment is of primary interest. The missed detection rate has been verified through extensive simulations as presented in Section 5.

The obtained data corresponds to typical in-service sensor measurements of a real commercial aircraft, with the sampling rate of typical flight control computers. The provided data sets include the desired control surface position (the command), generated by the Flight Control Laws, as well as the measured control surface position. Three different data sets have been delivered from different flight tests with the same aircraft type. The first data set is of a flight lasting more than one hour and starting with flight control checks on the ground, followed by many dynamic maneuvers until the cruise phase. The second data set is a complete but short flight, containing take-off and landing phases, in which steady maneuvers as well as dynamic maneuvers are performed. The third data set covers a highly dynamic flight phase. The evolution of the control surface deflection for the first data set is shown in Fig. 9(a). The other data sets are quantified in Table 3. One can see that all data sets comprise a large range of possible deflections and contain several highly dynamic flight phases.

The detection algorithm receives the pre-recorded flight data sequentially and calculates the thresholds and detection condition online. The detector is applied with the parameters from Table 2. In Fig. 9(b) the time-varying bounds on e used for detection are shown when applied to data set 1. An excerpt of a dynamic phase of the flight is highlighted, where it can be seen that the bounds more closely approach each other, but still no false detection occurs. To give some more insight into the evolution of the detection bounds, Table 3 presents some properties of $\tilde{e} - \underset{\sim}{e}$ also for the other data-sets. One can see that for all data sets $\tilde{e} - \underset{\sim}{e}$ comes close to 0, which is as expected considering the dynamic flight phases in each data set. However, no false alarm is triggered in any data set, which validates the robustness of the detection scheme.

6.1. Computational complexity

Computational complexity is important to determine the real-time applicability of the detection scheme on a commercial aircraft. Therefore the number of scalar operations, such as lookup tables, addition, multiplication, and logic operations, for each update of the detection scheme are counted. One update of the detector requires 120 scalar operations, of which 20 are used to update the SMO and the remaining 100 are used to construct the bounds on e and perform detection.

7. Conclusion

We have introduced a Sliding Mode Observer (SMO) based detection scheme for fast and reliable detection of oscillatory actuator failures in commercial aircrafts. Strong guarantees on both robustness and detection of the OFCs are presented. The detection scheme is by construction guaranteed to produce no false detection. Furthermore, the detection scheme provides guarantees on the minimum OFC amplitude as a function of OFC frequency that can be reliably detected within a specific maximum number of oscillation cycles of the fault. The maximum undetected OFC amplitude per frequency is related to the additional loads the OFC can cause and thus serves as an important input to the aircraft structural design. The detection scheme was verified in simulation and validated using real flight test data.

Monte-Carlo simulations were performed using a benchmark simulation of the actuator developed by Airbus and Stellenbosch University. The simulation results show that the detection scheme is able to consistently detect OFCs within a specified maximum number of cycles over the whole frequency range of 1–10 Hz, for both liquid and solid failures, and that originate at either the servo current input or at the rod position sensor. The OFC amplitude that can be consistently detected is a function of the OFC frequency, and is smaller at low frequencies than at high frequencies. Furthermore, no false detections were produced in any of the simulations, which shows that the detection scheme is robust to parameter uncertainty and external wind disturbances.

To validate the results obtained in simulation, the detection scheme was also applied to healthy flight test data provided by Airbus. No false detections were produced for any of the three different flight tests data sets, including a flight test of over one hour. This shows that the detection scheme is robust to practical parameter uncertainty, external wind disturbances, and aircraft maneuvers.

Some appealing avenues have been identified for future works, especially in view of a potential industrial use. First of all, an additional and more exhaustive validation campaign would be required. This comprehensive testing phase would allow to verify the robustness for a wider set of uncertainties for non-average and extreme situations and to verify the detection performances for additional configurations. This could be done in a first step on a more representative simulator (very high fidelity) and in a second step on real data. Another interesting perspective concerns the fault detection logic which is currently based on checking that the lower bound becomes greater than the upper bound. A more performant decision making step exploiting the difference of bounds behaviour in the faulty and fault-free situation could be investigated. Furthermore, the sliding mode observer (SMO)-based detection method utilizes an SMO which can simultaneously estimate the state and fault. This information that is inherently provided with the detection method has the potential to be used for fault identification and accommodation in the future. From the point of view of

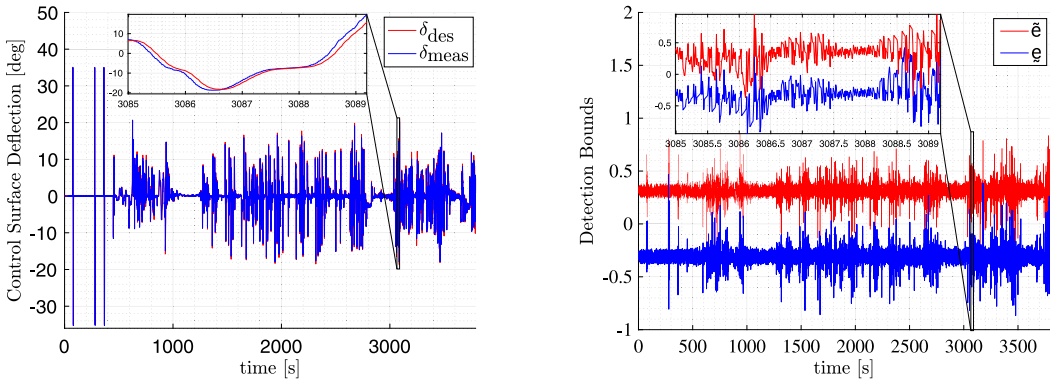

(a) Maneuvers performed to excite the system (b) Detection bounds indicating no false alarm

Fig. 9. Maneuvers and detector response during healthy behaviour of the performed flight test.

implementing the proposed algorithm on a real time platform, with limited CPU capacity, it would be interesting to study potential design simplification in view of alleviating the corresponding computational burden. The ultimate step would then be to code the proposed design on an industrial platform with a state-of-the-art and certified coding language for advanced tests on representative equipment (e.g. actuator test bench and real aircraft).

Declaration of competing interest

The authors declare that they have no known competing financial interests or personal relationships that could have appeared to influence the work reported in this paper.

Appendix A. Healthy system bounds

The expression for θ in Eq. (4) can be expanded to $\theta = \max(|\max_{\tilde{k}_d,\Delta\tilde{P},\tilde{k}_{\text{aero}},\Gamma,\xi_\delta,\xi_p}(\dot{p}^0) - \dot{p}_{\text{model}}|, |\min_{\tilde{k}_d,\Delta\tilde{P},\tilde{k}_{\text{aero}},\Gamma,\xi_\delta,\xi_p}(\dot{p}^0) - \dot{p}_{\text{model}}|)$, as $\dot{p}_{\text{model}}$ is not dependent on the uncertainties. In this way we only require to derive the bounds on $\dot{p}^0$ over all uncertainties to obtain θ. Based on Eq. (2) we will first derive bounds on V_c^0 and δ based on the uncertainty in the sensor noise. We will then use these bounds and the bounds on the uncertain model parameters to bound $\dot{p}^0$.

First note that the detector does not know p_{meas}, but needs to derive it from δ_{meas} using the relations in Eq. (1) as $p_{\text{meas}} = k_p^{-1}(\delta_{\text{meas}} - \xi_\delta) + \xi_p$. Using this relation and the definition of V_c^0 from Eq. (2) we can write $\underline{V}_c^0 \le V_c^0 \le \bar{V}_c^0$ where

$$\begin{aligned} \underline{V}_c^0 &= k_c(K(p_{\text{ref}} - (k_p^{-1}(\delta_{\text{meas}} + \bar{\xi}_\delta) - \bar{\xi}_p))), \\ \bar{V}_c^0 &= k_c(K(p_{\text{ref}} - (k_p^{-1}(\delta_{\text{meas}} - \bar{\xi}_\delta) + \bar{\xi}_p))). \end{aligned} \tag{A.1}$$

Furthermore, δ can be bound as

$$\delta_{\text{meas}} - \bar{\xi}_\delta = \underline{\delta} \le \delta \le \bar{\delta} = \delta_{\text{meas}} + \bar{\xi}_\delta \,. \tag{A.2}$$

Now we will bound $\dot{p}^0$, where we assume that all instances of V_c^0 appearing in Eq. (2) can be set independently to achieve the extremes. This results in

$$\begin{cases} \max(\dot{p}^0) \le \bar{V}_c^0 \sqrt{\dfrac{\max\limits_{\Delta\tilde{P}}(\Delta P) + \max\limits_{\tilde{k}_{\text{aero}}}(k_{\text{aero}})\max\limits_{\delta,V_c^0}(\frac{\delta \text{sgn}(V_c^0)}{S})}{\Delta P_{\text{ref}} + \min\limits_{\tilde{k}_d}(k_d)\min\limits_{V_c^0}(\frac{V_c^{0^2}}{S})}} + \max\limits_{\Gamma}(\Gamma) \text{ if } \bar{V}_c^0 > 0 \\ \max(\dot{p}^0) \le \bar{V}_c^0 \sqrt{\dfrac{\min\limits_{\Delta\tilde{P}}(\Delta P) + \min\limits_{\tilde{k}_{\text{aero}}}(k_{\text{aero}})\min\limits_{\delta,V_c^0}(\frac{\delta \text{sgn}(V_c^0)}{S})}{\Delta P_{\text{ref}} + \max\limits_{\tilde{k}_d}(k_d)\max\limits_{V_c^0}(\frac{V_c^{0^2}}{S})}} + \max\limits_{\Gamma}(\Gamma) \text{ if } \bar{V}_c^0 \le 0 \end{cases} \tag{A.3}$$

where $\max\limits_{\delta,V_c^0}(\delta \text{sgn}(V_c^0))$ and $\min\limits_{\delta,V_c^0}(\delta \text{sgn}(V_c^0))$ can be obtained by calculating the expression for all four combinations of the extremes of δ and V_c^0. Lastly, by Assumption 1, $\max_\Gamma(\Gamma) \le \gamma$.

Appendix B. Proof of Theorem 1

Proof (*Proposition 1*). Recall that we consider the healthy behaviour where $F = 0$. With $K_s = \theta + \eta$ we can define $V = \frac{e^2}{2}$ such that

$$\dot{V} = \dot{e}e = K_L e_{\text{meas}} e + \Theta e - (\theta + \eta)\text{sgn}(e_{\text{meas}})e \,. \tag{B.1}$$

Note that $e - e_{\text{meas}} = p - k_p^{-1}(\delta_{\text{meas}}) = p - k_p^{-1}(k_p(p) + \xi_\delta)$, such that if $e \ge \max_{p,\xi_\delta}(p - k_p^{-1}(k_p(p) + \xi_\delta)) \ge 0$ we have $e_{\text{meas}} \ge 0$ and we can simplify Eq. (B.1) to

$$\dot{V} \le (\Theta - (\theta + \eta))e \le -\eta e \le 0 \tag{B.2}$$

where $\dot{V} = 0$ iff $e = 0$ such that V is a Lyapunov function under healthy behaviour if $e \ge \max_{p,\xi_\delta}(p - k_p^{-1}(k_p(p) + \xi_\delta)) = \bar{e}^0$. In the same way it can be proven that V is a Lyapunov function if $e \le \min_{p,\xi_\delta}(p - k_p^{-1}(k_p(p) + \xi_\delta)) = \underline{e}^0 \le 0$. This means that under healthy behaviour e will converge to a region around the origin where $\underline{e}^0 \le e \le \bar{e}^0$. Furthermore, by initializing $\hat{p}$ as $\hat{p} = k_p^{-1}(\delta_{\text{meas}})$ we have $e = p - k_p^{-1}(\delta_{\text{meas}}) = p - k_p^{-1}(k_p(p) + \xi_\delta)$. So the derived bounds $\underline{e}^0 \le e \le \bar{e}^0$ hold also for the initial condition and therefore the bounds hold for all time.

From Eq. (6), with $F = 0$, one can derive $\bar{\dot{e}}^0$ as

$$\begin{aligned} |\dot{e}| =& |\Theta + K_L e_{\text{meas}} - (\theta + \eta)\text{sgn}(e_{\text{meas}})| \le |\Theta| + |K_L e_{\text{meas}}| \\ &+ |(\theta + \eta)\text{sgn}(e_{\text{meas}})| \\ &\le \theta + |K_L e_{\text{meas}}| + \theta + \eta = 2\theta + |K_L e_{\text{meas}}| + \eta = \bar{\dot{e}}^0 \end{aligned}$$

For $\underline{\dot{e}}^0$ we consider first that $e_{\text{meas}} > 0$, which by point 2 of this theorem means $\dot{e} < 0$. Therefore

$$|\dot{e}| = -\Theta - K_L e_{\text{meas}} + (\theta + \eta) \ge -K_L e_{\text{meas}} + \eta = |K_L e_{\text{meas}}| + \eta = \underline{\dot{e}}^0 \,,$$

where we use $K_L < 0$ and $\theta \ge |\Theta|$. Then consider that $e_{\text{meas}} < 0$, which by point 2 of this theorem means $\dot{e} > 0$. Therefore

$$|\dot{e}| = \Theta + K_L e_{\text{meas}} + (\theta + \eta) \ge K_L e_{\text{meas}} + \eta = |K_L e_{\text{meas}}| + \eta = \underline{\dot{e}}^0 \,,$$

where we again use $K_L < 0$ and $\theta \ge |\Theta|$. □

Proof (*Proposition 2*). From Eq. (6), with $F = 0$, we have

$$\begin{aligned} \text{sgn}(\dot{e}) =& \text{sgn}(\Theta + K_L e_{\text{meas}} - (\theta + \eta)\text{sgn}(e_{\text{meas}})) \\ =& \text{sgn}((\Theta - \theta\text{sgn}(e_{\text{meas}})) + K_L e_{\text{meas}} - \eta\text{sgn}(e_{\text{meas}})) \end{aligned}$$

where using $\theta \ge |\Theta|$, $K_L < 0$ and $\eta > 0$ for each additive term on the right-hand side it holds $\text{sgn}(\cdot) = -\text{sgn}(e_{\text{meas}})$, such that also $\text{sgn}(\dot{e}) = -\text{sgn}(e_{\text{meas}})$. □

Proof (*Proposition 3*). First, consider $e_{\text{meas}} > 0$, such that from Eq. (6) we have

$$\dot{e} = \Theta + F + K_L e_{\text{meas}} - (\theta + \eta) \leq K_L e_{\text{meas}} - \eta + F = \bar{\dot{e}}^+,$$
$$\dot{e} = \Theta + F + K_L e_{\text{meas}} - (\theta + \eta) \geq -2\theta + K_L e_{\text{meas}} - \eta + F = \underline{\dot{e}}^+.$$

Here we used $\theta \geq |\Theta|$. Then consider $e_{\text{meas}} < 0$, such that from Eq. (6) we have

$$\dot{e} = \Theta + F + K_L e_{\text{meas}} + (\theta + \eta) \leq 2\theta + K_L e_{\text{meas}} + \eta + F = \bar{\dot{e}}^-,$$
$$\dot{e} = \Theta + F + K_L e_{\text{meas}} + (\theta + \eta) \geq K_L e_{\text{meas}} + \eta + F = \underline{\dot{e}}^-.$$

Here we again used $\theta \geq |\Theta|$. □

Appendix C. Proof of robustness

Proof (*Robustness*). Define the sequence $\{t_{s_i}\}$ as the times where e_{meas} changes sign, and without loss of generality, assume e_{meas} becomes positive at every $t_{s_{2i}}$. Now we can define $\dot{e}_i^+$ as the average $\dot{e}$ during $\left[t_{s_{2i}},\ t_{s_{2i+1}}\right]$, and $\dot{e}_i^-$ as the average $\dot{e}$ during $\left[t_{s_{2i+1}},\ t_{s_{2i+2}}\right]$. Furthermore denote $t_i^+ = t_{s_{2i+1}} - t_{s_{2i}}$ and $t_i^- = t_{s_{2i+2}} - t_{s_{2i+1}}$. Note that superscript $^+$ denotes that e_{meas} is positive, which, by Theorem 1, means that $\dot{e}^+ < 0$ in healthy conditions. Similarly, in healthy conditions, $\dot{e}^- > 0$. Then, for analysis purposes, rewrite the continuous dynamics of e_2 from Eq. (6) in a discrete form based on the switching times as

$$e(t_{s_{2i+2N}}) = e(t_{s_{2i}}) + \sum_{j=0}^{N} c_{i+j} \ \forall N \in \mathbb{Z},$$
$$\text{where} \quad c_i \triangleq t_i^+ \dot{e}_i^+ + t_i^- \dot{e}_i^-,$$

where N is a counter that indicates the result holds for all time. Here c_i can be bounded in healthy conditions using Eq. (7) as

$$\max(e_{\text{meas}} + \underline{e}^0, \underline{e}^0) - e(t_{s_i}) \leq \sum_{j=0}^{N} c_{i+j} \leq \min(e_{\text{meas}} + \bar{e}^0, \bar{e}^0) - e(t_{s_i}) \ \forall N, i \in \mathbb{Z}. \tag{C.1}$$

Now, we will have a look at the dynamics of the bounds $\tilde{e}$ and $\underline{e}$ from Eq. (9). Without loss of generality, we will derive the dynamics of $\tilde{e}$ and $\underline{e}$ considering, individually, three situations that together describe its full dynamics.

1. $\tilde{e}$ and $\underline{e}$ are fully determined by the integral bounds in Eq. (8).
2. $\tilde{e}$ or $\underline{e}$ is affected by the static bounds in Eq. (7).
3. $\tilde{e}$ and $\underline{e}$ are both affected by the static bounds in Eq. (7).

For case 1, just looking at the integral bounds in Eq. (8), we can write

$$\tilde{e}(t_{s_{2i+2}}) = \tilde{e}(t_{s_{2i}}) - t_i^+ \underline{\dot{e}}^0 + t_i^- \bar{\dot{e}}^0. \tag{C.2}$$

From the definition of c_i it can be derived that $\frac{t_i^-}{t_i^+} = \frac{c_i}{t_i^+ \dot{e}_i^-} - \frac{\dot{e}_i^+}{\dot{e}_i^-}$, from which t_i^- can be substituted in Eq. (C.2) to obtain

$$\tilde{e}(t_{s_{2i+2}}) = \tilde{e}(t_{s_{2i}}) - \frac{t_i^+}{\dot{e}_i^-}(\bar{e}^0 \dot{e}_i^+ + \underline{\dot{e}}^0 \dot{e}_i^-) + \frac{\bar{e}^0}{\dot{e}_i^-} c_i.$$

This can be extended for $\tilde{e}(t_{s_{2i+2N}})$ as

$$\tilde{e}(t_{s_{2i+2N}}) = \tilde{e}(t_{s_{2i}}) + \sum_{j=0}^{N-1} \left(-\frac{t_{i+j}^+}{\dot{e}_{i+j}^-}(\bar{e}^0 \dot{e}_{i+j}^+ + \underline{\dot{e}}^0 \dot{e}_{i+j}^-) + \frac{\bar{e}^0}{\dot{e}_{i+j}^-} c_{i+j} \right). \tag{C.3}$$

for any $N \in \mathbb{Z}$. Similarly for $\underline{e}$ we can derive

$$\underline{e}(t_{s_{2i+2N}}) = \underline{e}(t_{s_{2i}}) + \sum_{j=0}^{N-1} \left(-\frac{t_{i+j}^+}{\dot{e}_{i+j}^-}(\underline{\dot{e}}^0 \dot{e}_{i+j}^+ + \bar{e}^0 \dot{e}_{i+j}^-) + \frac{\underline{\dot{e}}^0}{\dot{e}_{i+j}^-} c_{i+j} \right). \tag{C.4}$$

It can be seen that in healthy conditions, when $\underline{\dot{e}}^0 \leq \dot{e}_i^- \leq \bar{\dot{e}}^0$ and $-\bar{\dot{e}}^0 \leq \dot{e}_i^+ \leq -\underline{\dot{e}}^0$ for all i, then $(\bar{\dot{e}}^0 \dot{e}_{i+j}^+ + \underline{\dot{e}}^0 \dot{e}_{i+j}^-) \leq 0$ and $(\underline{\dot{e}}^0 \dot{e}_{i+j}^+ + \bar{\dot{e}}^0 \dot{e}_{i+j}^-) \geq 0$. Substituting this in Eqs. (C.3) and (C.4) the following inequalities can be obtained.

$$\begin{aligned} \tilde{e}(t_{s_{2i+2N}}) - \tilde{e}(t_{s_{2i}}) &\geq \sum_{j=0}^{N-1} \frac{\bar{e}^0}{\dot{e}_{i+j}^-} c_{i+j} \geq \sum_{j=0}^{N-1} c_{i+j}, \\ \underline{e}(t_{s_{2i+2N}}) - \underline{e}(t_{s_{2i}}) &\leq \sum_{j=0}^{N-1} \frac{\underline{e}^0}{\dot{e}_{i+j}^-} c_{i+j} \leq \sum_{j=0}^{N-1} c_{i+j}. \end{aligned} \tag{C.5}$$

Subtracting these inequalities gives $\tilde{e}(t_{s_{2i+2N}}) - \underline{e}(t_{s_{2i+2N}}) \geq \tilde{e}(t_{s_{2i}}) - \underline{e}(t_{s_{2i}})$. This proves that in healthy conditions, considering only the integral behaviour of case 1, the difference between $\tilde{e}$ and $\underline{e}$ is non-decreasing.

This only leaves to prove that in cases 2 and 3, the instantaneous update causes $\tilde{e} > \underline{e}$. In case 2, considering the lower bound is affected by the static bounds in Eq. (7), we have $\underline{e}(t_{s_{2i+2N}}) = \max(e_{\text{meas}} + \underline{e}^0, \underline{e}^0)$. Then using the first Equation in (C.5) we can write

$$\begin{aligned} \tilde{e}(t_{s_{2i+2N}}) \geq \tilde{e}(t_{s_{2i}}) + \sum_{j=0}^{N-1} c_{i+j} &\geq \tilde{e}(t_{s_{2i}}) + \max(e_{\text{meas}} + \underline{e}^0, \underline{e}^0) - e(t_{s_{2i}}) \\ &\geq \max(e_{\text{meas}} + \underline{e}^0, \underline{e}^0) = \underline{e}(t_{s_{2i+2N}}). \end{aligned}$$

In case 3 $\tilde{e} - \underline{e} = \bar{e}^0 - \underline{e}^0 - |e_{\text{meas}}| \geq 0$. □

Appendix D. Proof of detectability

Proof (*Lemma 1: Detectability*). First, use $\underline{\dot{e}}^0 > -\dot{e}_{i+j}^+ + \epsilon^+$ and $\bar{\dot{e}}^0 < \dot{e}_{i+j}^- - \epsilon^+ \ \forall i, j$ to derive

$$\begin{aligned} 0 = \underline{e}^0 \bar{e}^0 - \bar{e}^0 \underline{e}^0 &< \underline{e}^0(\dot{e}_{i+j}^- - \epsilon^+) - \bar{e}^0(-\dot{e}_{i+j}^+ + \epsilon^+) \\ -(\underline{e}^0 \dot{e}_{i+j}^- + \bar{e}^0 \dot{e}_{i+j}^+) &< -(\underline{e}^0 + \bar{e}^0)\epsilon^+. \end{aligned}$$

Then substitute this and $\phi \leq \frac{1}{\dot{e}_{i+j}^-} \ \forall i, j$ in Eq. (C.3) giving

$$\tilde{e}(t_{s_{2i+2N}}) - \tilde{e}(t_{s_{2i}}) \leq -(\underline{e}^0 + \bar{e}^0)\epsilon^+ \phi \sum_{j=0}^{N-1} t_{i+j}^+ + \sum_{j=0}^{N-1} \frac{\bar{e}^0}{\dot{e}_{i+j}^-} c_{i+j}.$$

Using the bound on c_{i+j} from Eq. (C.1), this gives

$$\begin{aligned} \tilde{e}(t_{s_{2i+2N}}) &< -(\underline{e}^0 + \bar{e}^0)\epsilon^+ \phi \sum_{j=0}^{N-1} t_{i+j}^+ + \min(e_{\text{meas}} + \bar{e}^0, \bar{e}^0) - e(t_{s_i}) + \tilde{e}(t_{s_{2i}}) \\ &\leq -(\underline{e}^0 + \bar{e}^0)\epsilon^+ \phi \sum_{j=0}^{N-1} t_{i+j}^+ + 2\min(e_{\text{meas}} + \bar{e}^0, \bar{e}^0) \\ &\quad - \max(e_{\text{meas}} + \underline{e}^0, \underline{e}^0) \end{aligned}$$

Meanwhile, always $\underline{e} \geq \max(e_{\text{meas}} + \underline{e}^0, \underline{e}^0)$, so

$$\begin{aligned} \tilde{e}(t_{s_{2i+2N}}) - \underline{e}(t_{s_{2i+2N}}) &< -(\underline{e}^0 + \bar{e}^0)\epsilon^+ \phi \sum_{j=0}^{N-1} t_{i+j}^+ + 2\min(e_{\text{meas}} + \bar{e}^0, \bar{e}^0) \\ &\quad - 2\max(e_{\text{meas}} + \underline{e}^0, \underline{e}^0) \\ &= -(\underline{e}^0 + \bar{e}^0)\epsilon^+ \phi \sum_{j=0}^{N-1} t_{i+j}^+ + 2(\bar{e}^0 - \underline{e}^0 - |e_{\text{meas}}|) \end{aligned}$$

This means that $\tilde{e}(t_{s_{2i+2N}}) < \underline{e}(t_{s_{2i+2N}})$ if $(\underline{e}^0 + \bar{e}^0)\epsilon^+ \phi \sum_{j=0}^{N-1} t_{i+j}^+ \geq 2(\bar{e}^0 - \underline{e}^0 - |e_{\text{meas}}|)$, or equivalently $\sum_{j=0}^{N-1} t_{i+j}^+ \geq \frac{2(\bar{e}^0 - \underline{e}^0 - |e_{\text{meas}}|)}{(\underline{e}^0 + \bar{e}^0)\epsilon^+ \phi}$.

Similarly we can obtain $\sum_{j=0}^{N-1} t_{i+j}^+ \geq \frac{2(\bar{e}^0 - \underline{e}^0 - |e_{\text{meas}}|)}{(\underline{e}^0 + \bar{e}^0)\epsilon^- \phi}$ using $\bar{e}^0 < -\dot{e}_{i+j}^+ - \epsilon^-$ and $\underline{e}^0 > \dot{e}_{i+j}^- + \epsilon^-$. To this end derive $-(\underline{e}^0 \dot{e}_{i+j}^+ + \bar{e}^0 \dot{e}_{i+j}^-) > (\underline{e}^0 + \bar{e}^0)\epsilon^-$ and substitute in Eq. (C.4). □

References

Alcorta-Garcia, E., Zolghadri, A., & Goupil, P. (2011). A nonlinear observer-based strategy for aircraft oscillatory failure detection: A380 case study. *IEEE Transactions on Aerospace and Electronic Systems*, *47*(4), 2792–2806.

Alwi, H., & Edwards, C. (2013). An adaptive sliding mode differentiator for actuator oscillatory failure case reconstruction. *Automatica*, *49*(2), 642–651. http://dx.doi.org/10.1016/j.automatica.2012.11.042.

Besch, H. M., Giesseler, H. G., & Schuller, J. (1996). *Impact of electronic flight control system failure cases on structural design loads: Tech. rep.*, AGARD 815, Loads and Requirements for Military Aircraft.

Chen, H., Jiang, B., Ding, S. X., & Huang, B. (2022). Data-driven fault diagnosis for traction systems in high-speed trains: A survey, challenges, and perspectives. *IEEE Transactions on Intelligent Transportation Systems*, *23*(3), 1700–1716. http://dx.doi.org/10.1109/TITS.2020.3029946.

Chi, Y., Dong, Y., Wang, Z. J., Yu, F. R., & Leung, V. C. M. (2022). Knowledge-based fault diagnosis in industrial internet of things: A survey. *IEEE Internet of Things Journal*, *9*(15), 12886–12900. http://dx.doi.org/10.1109/JIOT.2022.3163606.

Cieslak, J., Efimov, D., Zolghadri, A., Henry, D., & Goupil, P. (2013). Oscillatory failure case detection for aircraft using non-homogeneous differentiator in noisy environment. In *2nd CEAS specialist conference on guidance, navigation & control* (pp. 394–413).

Edwards, C., Spurgeon, S. K., & Patton, R. J. (2000). Sliding mode observers for fault detection and isolation. *Automatica*, *36*, 541–553.

Efimov, D., Cieslak, J., Zolghadri, A., & Henry, D. (2013). Actuator fault detection in aircraft systems: Oscillatory failure case study. *Annual Reviews in Control*, *37*(1), 180–190.

Frank, P. M. (1990). Fault diagnosis in dynamic systems using analytical and knowledge-based redundancy: A survey and some new results. *Automatica*, *26*(3), 459–474. http://dx.doi.org/10.1016/0005-1098(90)90018-D.

Frank, P., & Ding, X. (1997). Survey of robust residual generation and evaluation methods in observer-based fault detection systems. *Journal of Process Control*, *7*(6), 403–424. http://dx.doi.org/10.1016/S0959-1524(97)00016-4.

Goupil, P. (2010). Oscillatory failure case detection in the A380 electrical flight control system by analytical redundancy. *Control Engineering Practice*, *18*(9), 1110–1119.

Goupil, P., Urbano, S., & Tourneret, J.-Y. (2016). A data-driven approach to detect faults in the airbus flight control system. *IFAC-PapersOnLine*, *49*(17), 52–57.

Hwang, I., Kim, S., Kim, Y., & Seah, C. E. (2010). A survey of fault detection, isolation, and reconfiguration methods. *IEEE Transactions on Control Systems Technology*, *18*, 636–653. http://dx.doi.org/10.1109/TCST.2009.2026285.

Lavigne, L., Cazaurang, F., Fadiga, L., & Goupil, P. (2014). New sequential probability ratio test: Validation on A380 flight data. *Control Engineering Practice*, *22*, 1–9.

Lavigne, L., Zolghadri, A., Goupil, P., & Simon, P. (2011). A model-based technique for early and robust detection of oscillatory failure case in A380 actuators. *International Journal of Control, Automation and Systems*, *9*(1), 42–49.

Loutridis, S. (2004). Damage detection in gear systems using empirical mode decomposition. *Engineering Structures*, *26*(12), 1833–1841.

Mahrukh, & Liaqat, M. (2018). Fault reconstruction using sliding mode observer for LTI systems: A survey. In *2018 IEEE 9th annual information technology, electronics and mobile communication conference* (pp. 945–949). http://dx.doi.org/10.1109/IEMCON.2018.8615018.

Mohammadi, A., Marquez, H. J., & Tavakoli, M. (2017). Nonlinear disturbance observers: Design and applications to Euler-Lagrange systems. *IEEE Control Systems Magazine*, *37*(4), 50–72. http://dx.doi.org/10.1109/MCS.2017.2696760.

Narendra, K. S., & Balakrishnan, J. (1997). Adaptive control using multiple models. *IEEE Transactions on Automatic Control*, *42*(2), 171–187.

Pons, R., Jauberthie, C., Travé-Massuyès, L., & Goupil, P. (2008). Interval analysis based learning for fault model identification. application to control surfaces oscillatory failures. In E. Bradley, & L. Travé-Massuyès (Eds.), *22nd International workshop on qualitative reasoning* (pp. 115–122). Boulder, CO, USA: University of Colorado.

Sachs, H., Carl, U. B., & Thielecke, F. (2007). An approach to the investigation of oscillatory failure cases in electro-hydraulic actuation systems. In *Recent advances in aerospace actuation systems and components* (pp. 99–104). Toulouse, France.

Sifi, M., Lavigne, L., Cazaurang, F., & Goupil, P. (2012). Oscillatory failure detection in flight control system of civil aircraft: EHA actuator servo loop case study.. In *R3ASC'12 (Recent advances in aerospace actuation systems and components)* (pp. 55–64).

Song, J., & He, X. (2022). Model-based fault diagnosis of networked systems: A survey. *Asian Journal of Control*, *24*(2), 526–536. http://dx.doi.org/10.1002/asjc.2543.

Spurgeon, S. K. (2008). Sliding mode observers: A survey. *International Journal of Systems Science*, *39*(8), 751–764. http://dx.doi.org/10.1080/00207720701847638.

Sun, X., Patton, R. J., & Goupil, P. (2012). Robust adaptive fault estimation for a commercial aircraft oscillatory fault scenario. In *Proceedings of 2012 UKACC international conference on control* (pp. 595–600). IEEE.

Tipaldi, M., & Bruenjes, B. (2015). Survey on fault detection, isolation, and recovery strategies in the space domain. *Journal of Aerospace Information Systems*, *12*(2), 235–256. http://dx.doi.org/10.2514/1.I010307.

Trinh, D. H., Marx, B., Goupil, P., & Ragot, J. (2014). Oscillatory failure detection in the flight control system of a civil aircraft using soft sensors. *New Sensors and Processing Chain*, 85–105.

Urbano, S., Chaumette, E., Goupil, P., & Tourneret, J. (2017). A data-driven approach for actuator servo loop failure detection. *IFAC-PapersOnLine*, *50*(1), 13544–13549.

Utkin, V. (1977). Variable structure systems with sliding modes. *IEEE Transactions on Automatic Control*, *22*(2), 212–222. http://dx.doi.org/10.1109/TAC.1977.1101446.

Varga, A., & Ossmann, D. (2012). LPV-model based identification approach of oscillatory failure cases. In *IFAC international symposium on fault detection, supervision and safety of technical processes* (pp. 1347–1352). Mexico City, Mexico.

Varga, A., & Ossmann, D. (2014). LPV model-based robust diagnosis of flight actuator faults. *Control Engineering Practice*, *31*, 135–147.

Yutian, L., Changgang, L., & Junjie, H. (2010). Fault diagnosis and fault tolerant control of nonlinear systems. In *2010 IEEE international conference on automation and logistics* (pp. 447–450). http://dx.doi.org/10.1109/ICAL.2010.5585326.

Zolghadri, A., Henry, D., Cieslak, J., Efimov, D., & Goupil, P. (2013). Fault diagnosis and fault-tolerant control and guidance for aerospace vehicles: From theory to application. In *Advances in industrial control*, (p. 216). Springer London Ltd, http://dx.doi.org/10.1007/978-1-4471-5313-9, URL https://hal.archives-ouvertes.fr/hal-00869253.